Real time X-ray diffraction imaging for semiconductor wafer metrology and high temperature in-situ experiments

A. N. Danilewsky[(1)], J. Wittge[(1)], A. Hess[(1)], A. Cröll[(1)], A. Rack[(2)],
D. Allen[(3)], P. McNally[(3)], T. dos Santos Rolo[(4)], P. Vagovič[(4)], T. Baumbach[(4)],
J. Garagorri[(5)], M.R. Elizalde[(5)] and B.K.Tanner[(6)]

Abstract

We describe a rapid digital system for X-ray diffraction imaging.and demonstrate its application to the real-time identification of edge defects in a silicon wafer that had been subjected to rapid thermal annealing. The application of the system to the *in situ* study of slip nucleation at the location of mechanical wafer defects, indents and a thermocouple, and the subsequent dislocation dynamics is presented.

1 Introduction

X-Ray diffraction imaging (topography) has been used for over half a century for the characterization of extended defects such as dislocations, slip bands, stacking faults, etc. in single crystals and devices fabricated thereupon [1]. X-ray sensitive films of sufficiently small grain size to give high resolution need exposure times ranging from seconds to minutes even if high intensity radiation from a synchrotron light source is used. They typically require a 10-20 minutes development procedure, which makes time resolved experiments difficult. The problem can be overcome by using CCD-camera systems which consist of a thin scintillating single crystal, an optical system and a digital camera [2].

Live X-ray diffraction topography using laboratory sources was pioneered in the 1960s, e.g. by applying modified television cameras as X-ray imaging detectors [3]. In those

early experiments the X-ray photons directly created an electron-based signal and this concept is nowadays more generally called direct detection. During the 1970s there was development of indirect X-ray imaging detectors where the luminescence image from a scintillator screen is projected by visible light optics onto a camera [4]. At the same time, X-ray diffraction topography was successfully performed by employing hard X-ray synchrotron radiation [5]. The first experiments combining synchrotron radiation and live topography were reported in the 1980s by Tuomi *et al.* [6], over which period Chikawa continued to improve his system with a conventional source [7].

In general, direct detectors offer higher efficiency but have poorer dynamic range and resolution compared to indirect detection systems. By use of magnifying optics between the scintillator and camera, the latter enables (sub-)micrometre spatial resolutions to be reached. However, for such high resolution, the scintillator must be very thin, and hence inefficient. As the Rose-de Vries law constrains intensity, efficiency, resolution, signal-to-noise and signal integration time, there has been much development over the last decade in high efficiency single crystal scintillators with low light scattering in the scintillator itself [8,9]. Despite their limited fields of view, indirect X-ray imaging detectors have proven to be well suited for digital synchrotron X-ray topography for industrial applications, e.g. the mapping of defects in large silicon wafers up to 300 mm in diameter [10]. More details on high resolution X-ray detectors can be found in refs [11,12].

2 Experimental

All experiments described here were carried out at the bending-magnet beamline Topo-Tomo of the German light source ANKA (ANgströmquelle KArlsruhe, a division of the Karlsruhe Institute of Technology). This is a 2.5 GeV storage ring which started operating in 2000 with first user experiments around 2003 [13]. Detailed descriptions of the beamline and the experimental stations are published elsewhere [9,14]. For topography experiments, Topo-Tomo is operated in white-beam mode. Here, the only mandatory optical element is the vacuum exit window (0.5-mm-thick polished beryllium, 28 m from the source point). Thus, a broad energy spectrum is accessible for the experiment (roughly from 6 keV to 30 keV at the position of the experiment) in combination with a highly homogeneous beam profile. The “BAMline macroscope” available at Topo-Tomo was employed as a high resolution indirect X-ray imaging detector [15] for the digital topography measurements [2]. Its design is based

on the concepts of Hartmann *et al.* [4] as well as Bonse and Busch [16]; the luminescence image of a scintillator screen is coupled via diffraction limited visible light optics to a camera (CCD or CMOS). For the experiment, the macroscope was equipped with a Rodenstock TV-Heliflex objective (f = 50 mm, max. NA = 0.45), a Nikkor 180/2.8 ED (f = 180 mm) objective as tube lens, a pco.4000 CCD camera (4008 × 2672 pixels, 9 μm in size) and a 25 mm × 25 mm $CdWO_4$ (CWO) or Ce-doped $Lu_3Al_5O_{12}$ (LuAG) polished scintillator single crystals. They are 300-μm-thick giving, at 3.6x magnification, a 2.5 μm effective pixel size and spatial resolution R < 5 μm in a 10.0 mm × 6.7 mm field of view, [17,18]. Due to the high stopping power of the CWO crystal in combination with the light collection efficiency of the Rodenstock objective permits live imaging by cineradiography of living insects with frame rates up to 250 images/s, as already demonstrated at Topo-Tomo [19]. For our experiments, the pco.4000 camera with a Kodak KAI-11000 interline transfer chip gave access to frame rates of up to 5 images/s in full-frame mode (depending on the dynamic range). Higher frame rates up to 40 frames per second are achievable when working with a limited region of interest.

The small size of the scintillating crystals compared to the typical dimensions of X-ray films of approx. 13 x 18 cm^2 available, limits the field of view to one single topograph and for silicon the $0\bar{2}2$ reflection was chosen. Improved resolution and sensitivity permits continuous imaging at frequencies of about 1-10 Hz whilst maintaining adequate topographic resolution. This reduction of the camera integration time allows us to achieve a near real time metrology of large wafers with high speed. When used with a heating system the *in-situ* study of dislocation dynamics becomes possible without blurring effects and with high time resolution [20]. Mirror heaters [21] allow *in situ* experiments at high temperature to be undertaken straightforwardly, e.g. tomography [22] ,as well as diffraction imaging [20,23,24].

For the *ex-situ* experiments discussed in this paper a 200mm diameter Si wafer was plateau annealed for 60 seconds at 1000°C and then characterised in real time using the 300mm wafer translation stage at the Topo-Tomo beamline (Fig1). For the *in-situ* experiment a 20 x 20 mm^2 Si slice with seven artificially produced defects from a 2N load of a Vickers tipped indenter was used [25]. The defects were aligned along the [011] direction and adjusted vertically inside the heater which is the direction of the strongest temperature gradient [20]. Plateau annealing up to approx. 1000 °C was controlled with 2 thermocouples at the back side of the sample. The diffraction images from the *in-situ* heating experiment were recorded by the camera system at a frame rate of 5 Hz.

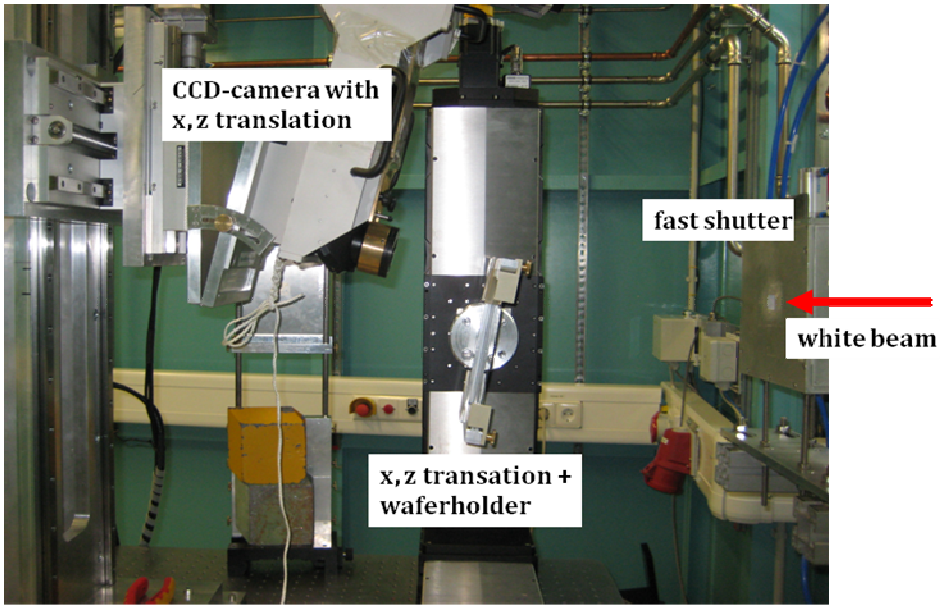

Figure 1 Experimantal set-up for diffraction imaging of the Topo-Tomo beamline, ANKA with a 200 mm Si wafer tilzted by 12° for a mapping of the $0\bar{2}2$ reflection with the digital camera system. The x-,z-translation stages can be replaced by larger one for 450mm Si-wafers or by a heater for the *in-situ* experiments.

3 Results and Discussion

From the study of full wafer X-ray diffraction images, such as found in ref. [26], it becomes evident that after high temperature annealing, an originally dislocation free wafer shows a high number of dislocations and slip bands which originate at the wafer edge. All the slip bands run in <110> directions in the (100) surface as it is expected for the diamond structure with {111} slip systems. The analysis of a number of wafer maps with different heating profiles shows that the length of a slip band is a function of the time the temperature stays above the brittle-ductile transition of silicon.

Table 1 compares the times needed to aquire complete maps of wafers with different wafer diameters at the Topo-Tomo beamline using the $0\bar{2}2$ reflection and a beam size of 5 x 8 mm^2 with the digital camera system set for an integration time of 0.1 second.

Table 1 Process time for complete wafer mapping at Topo-Tomo beamline, ANKA , $0\bar{2}2$ reflection, transmission mode, 5 x 8 mm^2 beam size.

Diameter:	200 mm	300 mm	450 mm*
Area [mm^2]	31416	70686	159043
Images	655	1767	3976
Integration time [s]	0.1	0.1	0.1
Motors + camera movement [s]	3.8	3.8	3.8
Total time [h]	0.7	1.9	4.3

*calculated

Fig. 2 shows four topographs from a complete edge region survey of a typical 200 mm Si wafer performed at the Topo-Tomo beamline ANKA. The wafer, originally dislocation free, shows a high number of extended defects after a 60 second plateau anneal, originating mainly at the wafer edge. In fig. 2a we show the start of the *ex-situ* survey at the notch with topograph no. 0000 at 0 sec and the movie shows the sequence of topographs around the complete wafer edge. A frame rate of 40 frames per second results, after processing and dark correction on 8 images, in an effective exposure time of 0.2 seconds. The clearness of the laser label in fig. 2a is a sign of the high spatial resolution which is achieved with this 0.2 s integration time. Dense slip bands originate directly from the notch. From the geometric analysis and additional topographs with various diffraction vectors recorded on high resolution X-ray film, it is concluded that the slip bands consist of 60° dislocations of the type **b** = a/2<110> mainly in pairs of opposite inclined {111} glide planes [23]. Single 60° dislocations can be resolved in the lower single slip band which is located at some distance from the edge. Due to the perpendicular <110> orientations of the slip bands they may cross at some distance towards the wafer's edge as shown in figure 2b, topograph no. 0840 after 168 s. These slip bands originate mainly at defects at the wafer's edge, which is shown in fig. 2c, topograph no. 1630 after 326 s of scanning. Finally a scan across a diagonal direction over the wafer shows some line defects near the centre of the wafer (fig. 2d, topograph no. 2210 after 442 s).

The sub-second integration time for data capture not only allows us to examine the defect structure in the wafer in real time, steering the field of view into a region of interest, but also enables us to capture details of dislocation motion at high velocity. We present an example of studies of motion of dislocations and slip bands nucleated at indents during high temperature annealing in the mirror furnace.

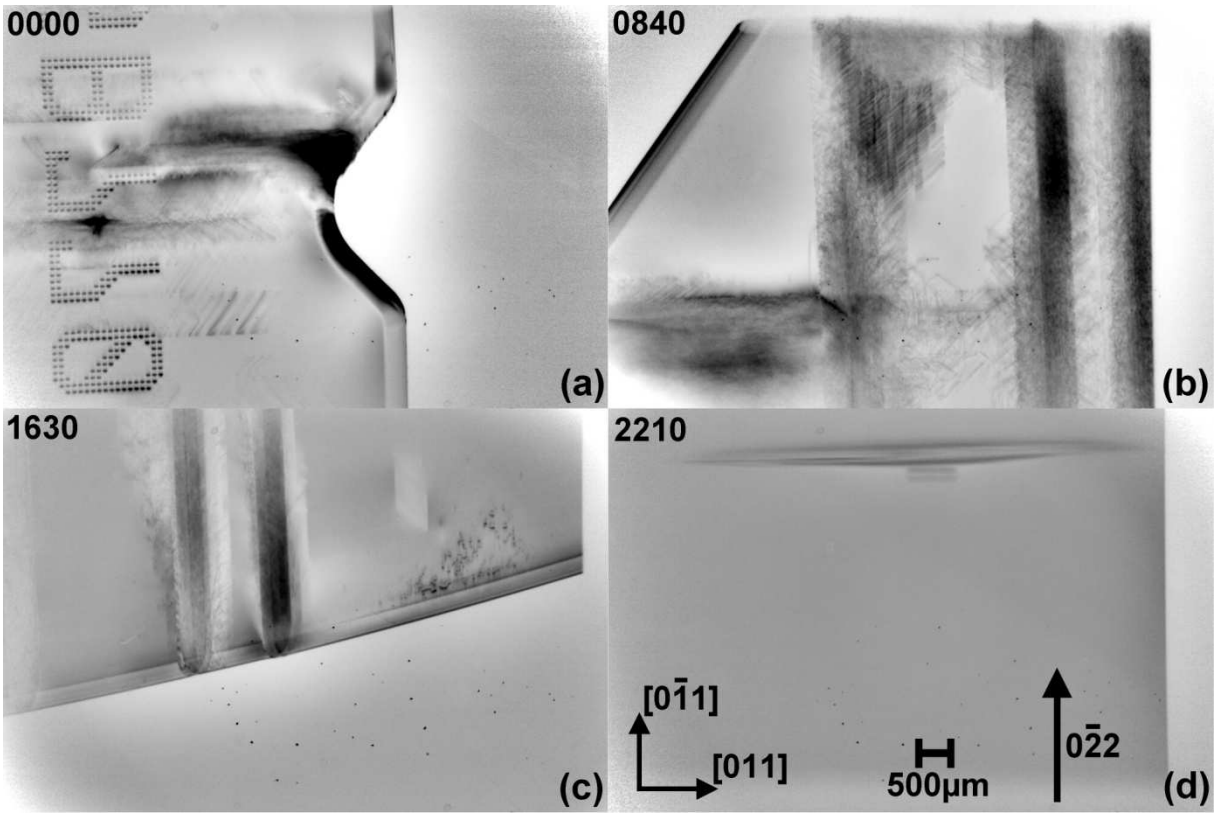

Figure 2 X-ray diffraction imaging metrology of 200 mm Si wafer (no. 07). Ex-situ at room temperature after 60 seconds plateau annealing at 1000 °C

(a) t = 0 sec topograph no. 0: Laser label and slip bands originating from the notch
(b) t = 168 sec topograph no. 0840: Crossing of <110> slip bands from the wafers edge
(c) t = 326 sec topograph no. 1630: <110> slip bands from the wafers edge and defects without dislocation loop formation
(d) t = 442 sec topograph no. 2210: Defect near the centre of a widely dislocation free area

Fig. 3 shows a series of five topographs taken from an *in-situ* movie of plateau annealing of a 20 x 20mm^2 square cut from a 200 mm (100) Si wafer. For this experiment seven indents were aligned vertically and parallel to the [011] direction which is the direction of the highest temperature gradient, of about 180°C/cm, inside the heater. At room temperature before heating, strong contrast related to the strain fields around the indents is visible in fig. 3a. The white contrast is absorption contrast belonging to the shadow of the upper thermocouple which was touching the back side of the sample for temperature control. During heating, the size of the strain fields reduced because of an annealing effect (fig. 3b) when a high density of dislocations was created beneath the indent. This dislocation array is below the resolution of X-ray topography but is visible in scanning transmission electron microscope images [25].

The time when the first dislocation loops became visible in the topographs was defined to be 0 s in fig. 3b.

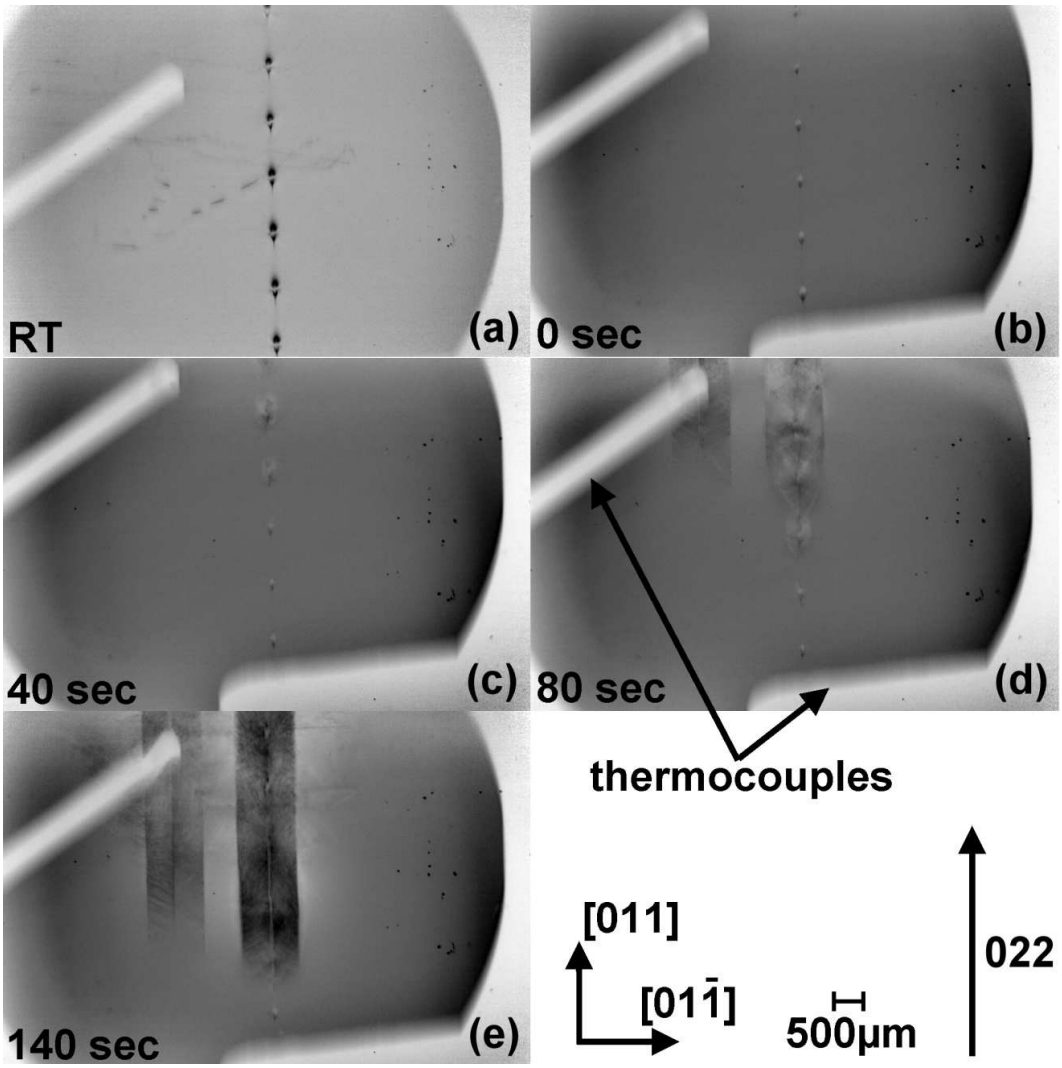

Figure 3 X-ray diffraction imaging metrology of Si wafer (no. Br7, 2N indents, 20 x 20 mm^2) in-situ at room temperature during plateau annealing up to 1000 °C

(a) Topograph taken at room temperature before the heating:
Contrasts from large strain fields around the indents
(b) t = 0 s at about 960°C: Size of strain fields reduced, first dislocation loops become visible
(c) t = 40 s topograph at about 968 °C: Upper dislocation loops at higher temperature increase faster in size
(d) t = 80 s topograph at 975 °C: Slip bands from adjacent indents overlap , no increase of dislocations loops at low temperature. Slip band starts to develop at the thermocouple.
(e) t = 140 s topograph at about 1000°C: Strong pairs of slip bands parallel [011] direction from indents and the thermocouple, horizontal slip bands parallel [01$\bar{1}$] only from upper indents at higher temperature. Around the lower indents at about 850 °C only single dislocation loops with small diameter develop

Due to a slight change in the diffraction conditions during the heating to about 960°C at the upper thermocouple, the position of the field of view moved slightly and the lower thermocouple becams visible too. For an upper thermocouple reading of 960°C, the lower thermocouple read 815°C and at this stage, the heating power was kept constant. As a result of the heat flows the temperature still slowly increased. The dislocation loops increased in

size and new dislocation loops originated at the position of the indents. The change of the position of the gliding dislocation segments can be measured from frame to frame and, knowing the time between frames, the dislocation velocity can be calculated. Because of the higher speed of the dislocations at higher temperature, the increase in size of the dislocation loops was greatest near the upper thermocouple. The highest speed of a 60° segment in a dislocation loop near the top thermocouple was measured to be 1.6 x 10^{-5} m/s, whereas the velocity was found to be between 3.8 and 6.4 x 10^{-6} m/s at the lower indents close to the lower thermocouple at temperature 815 °C. For the screw segments the velocity was determined to be 1.4 x 10^{-5} m/s and between 2.9 and 3.5 x 10^{-6} m/s for high and low temperature loops, respectively. This value is slightly lower than the corresponding 60° dislocations and is in good agreement with our earlier measurements [24]. After 80 seconds (fig. 3d) we observed that the dislocations originating from the upper indents cross and resulted in complex interactions, whereas the dislocation loops around the lower indents still increased slowly in size with a consistently slower speed. It has to be noted, that at this stage dislocation loops were also observed which originate from the position where the thermocouple touched the sample. The contact of a metal with large thermal conductivity produces a heat sink. Because no additional pressure is applied, the driving force is a local temperature gradient due to the heat flow through the thermocouple. Finally after 140 s, two dense pairs of {111} slip bands were formed parallel to the [011] direction. Horizontal slip bands along $[0\bar{1}1]$ were only formed at the upper indents. Due to the smaller horizontal temperature gradient of about 80°C/cm the slip bands were less dense with lower contrast and within them single dislocations can be resolved. Finally, during the fast cooling down, a high number dislocations originated but, due to the overall high dislocation density, the interpretation of the complex interactions is not so far possible. .

3 Conclusions

In summary it can be concluded that the increased sensitivity of digital camera systems allows real time X-ray diffraction imaging, with sub-second integration time, to be undertaken with a spatial resolution similar to high resolution X-ray film. One application is the fast metrology of large wafers at room temperature, while another is the observation of dynamical processes at high and changing temperatures, where the short integration time reduces the blurring of the topographs as a result of the high dislocation velocities and changes in the lattice constant of the crystal.

We have observed that temperature gradients during heating and cooling as well as heat sinks associated with thermocouple contact produce local temperature gradients in a sample and these act as sources of dislocation loops and slip bands. This correlates well with our finding that the highest speed and preferred propagation of dislocations is always in the direction of the highest temperature gradient [20,23]. The mechanical defects which act as sources for dislocation loops are located at the notch, the wafers edges and the bevel edges [26] and are all remnants of the mechanical manufacturing of a wafer or from its handling.

From heating experiments with different heating profiles and samples with different, well defined, artificially produced defects it is concluded that slip bands are formed from dislocation rings when the screw segments slip out at the back side of a wafer. The hold time above the critical temperature for the brittle-ductile transition defines the length of a slip band [24,26] as the velocity is observed to be constant. With increasing loading force for an indent, the size of the defects and the spatial extent of the surrounding strain field increases [25]. A graeter number of parallel slip systems can be activated resulting in complex dislocation patterns of dense slip systems such as shown in fig. 3e. Applied forces below approx. 200 mN produced no dislocations [26]. Above 400 mN indent loads single dislocation loops and above 2 N a high number of dislocation loops in parallel glide plane systems develop [23,24]. Looking at the black contrast features in fig. 2c which have not developed dislocation loops or slip bands, it can to be concluded that the original defects corresponded to defects corresponding to forces smaller than 200 mN.

Acknowledgements

Financial support was provided through the European Community FP7 STREP project SIDAM (Grant No. 216382). P. McNally acknowledges the assistance of the Irish Higher Education Authority PRTLI "INSPIRE" project and the Science Foundation Ireland "Precision" Strategic Research Cluster. Technical support by W. Drayer and H. Schade at Kristallographie Freiburg and ANKA (ISS, KIT Karlsruhe) respectively is gratefully acknowledged.

References

[1] D. K. Bowen and B. K. Tanner, X-ray Metrology in Semiconductor Manufacturing (CRC Taylor and Francis, Boca Raton, 2006).
[2] A. N. Danilewsky, A. Rack, J. Wittge, T. Weitkamp, R. Simon, H. Riesemeier, and T. Baumbach, Nucl. Instr. Meth. Phys. B **266**, 2035-2040 (2008).
[3] J.-I. Chikawa and I Fujimoto, Appl. Phys. Lett. **13**, 387–389 (1968).
[4] W. Hartmann, G. Markewitz, U. Rettenmaier, and H. J. Queisser, Appl. Phys. Lett. **27**, 308–309 (1975).
[5] T. Tuomi, K. Naukkarinen, and P. Rabe, phys. stat. sol. (a) **25**, 93 (1974).
[6] T. Tuomi, V. Kelhä, and M. Blomberg, Nucl. Instr. & Meth. **208**, 697–700 (1983).
[7] J. Chikawa, Proc. Jpn. Acad. Ser. B **80,** 317-326 (2004).
[8] A. Koch, C. Raven, P. Spanne, and A. Snigirev, J. Opt. Soc. Am. **15**, 1940–1951 (1998).
[9] A. Rack, F. Garcia-Moreno, T. Baumbach, and J. Banhart, J. Synchrotron Radiat. **16**, 432–434 (2009).
[10] A. N. Danilewsky, J. Wittge, A. Rack, T. Weitkamp, R. Simon, P. McNally, J. Mater. Sci.: Mater. Electron. **19**, 269–272 (2008).
[11] H. Graafsma and T. Martin, in: Advanced Tomographic Methods in Materials Research and Engineering edited by J. Banhart (Oxford University Press, 2008), pp. 277–302.
[12] S. M. Gruner, M. W. Tate, and E. F. Eikenberry, Rev. Sci. Instrum. **73**, 2815–2842 (2002).
[13] H. O.Moser, J. Alloy. Compd. **328**, 42–49 (2001).
[14] A. N. Danilewsky, R. Simon, A. Fauler, M. Fiederle, and K. W. Benz, Nucl. Instr. & Meth. in Phys. Res. B **199**, 71–74 (2003).
[15] A. Rack, S. Zabler, B. R. Müller, H. Riesemeier, G. Weidemann, A. Lange, J. Goebbels, M. Hentschel, and W. Görner, Nucl. Instr. & Meth. in Phys. Res. A **586**, 327–344 (2008).
[16] U. Bonse and F. Busch, Prog. Biophys. Molec. Biol. **65**, 133–169 (1996).
[17] L. Nagornaya, G. Onyshchenko, E. Pirogov, N. Starzhinskiy, I. Tupitsyna, V. Ryzhikov, Y. Galich, Y. Vostretsov, S. Galkin, and E. Voronkin, Nucl. Instrum. & Meth. in Phys. Res. A **537**, 163–167 (2005).
[18] A. Rack, T. Weitkamp, S. Bauer Trabelsi, P. Modregger, A. Cecilia, T. dos Santos Rolo, T. Rack, D. Haas, R. Simon, R. Heldele, M. Schulz, B. Mayzel, A. N. Danilewsky, T. Waterstradt, W. Diete, H. Riesemeier, B. R. Müller, and T. Baumbach, Nucl. Instr. & Meth. in Phys. Res. B **267**, 1978–1988 (2009).
[19] A. Rack, F. Garcia-Moreno, C. Schmitt, O. Betz, A. Cecilia, A. Ershov, T. Rack, J. Banhart, and S. Zabler, J. X-ray Sci. Techn. **18**, 429–441 (2010).
[20**]** A. Danilewsky, J. Wittge, A. Hess, A. Cröll, D. Allen, P. McNally, P. Vagovic, A. Cecilia, Z. Li, T. Baumbach, E. Gorostegui-Colinas, and M. R. Elizalde, Nucl. Instrum. & Meth. Phys. B **268**, 399-402 (2010.
[21] A. Eyer, R. Nietsche, and H. Zimmermann, J. Cryst. Growth **47**, 219-229 (1979).
[22] R. Grupp, F. Henkel, M. Nöthe, J. Banhart, B. Kieback, A. Haibel, J. Synchrotron. Radiat. **16**, 524-527 (2009).
[23] J. Wittge, A. N. Danilewsky, D. Allen, P. McNally, Z. Li, T. Baumbach, E. Gorostegui-Colinas, J. Garagorri, M. R. Elizalde, D. Jaques, M. C. Fossati, D. K. Bowen, and B. Tanner, J. Appl. Cryst. **43**, 1036-1039 (2010).
[24] A. N. Danilewsky, J. Wittge, A. Hess, A. Croell, D. Allen, P. McNally, P. Vagovic, T. dos Santos Rolo, Z. Li, T. Baumbach, E. Gorostegui-Colinas, J. Garagorri, M. R. Elizalde, M. Fossati, D. K. Bowen, and B. Tanner, J. Crystal Growth, *in press* (2010), 10.1016/j.jcrysgro.2010.10.199.
[25] J. Garagorri, E. Gorostegui-Colinas, M.R. Elizalde, D. Allen, and P. McNally, Anales de Mecánica de la Fractura **27**, 559-564 (2010).
[26] J. Wittge, A. N. Danilewsky, D. Allen, P. McNally, Z. Li, T. Baumbach, E. Gorostegui-Colinas, J. Garagorri, M. R. Elizalde, D. Jaques, M. C. Fossati, D. K. Bowen, and B. Tanner, Powder Diffraction **25**, 99-103 (2010).